Journal of Magnetism and Magnetic Materials 521 (2021) 167324

Contents lists available at ScienceDirect

Journal of Magnetism and Magnetic Materials

journal homepage: www.elsevier.com/locate/jmmm

Research articles

Enhanced magnetic signal along edges of embedded epitaxial $La_{0.7}Sr_{0.3}MnO_3$ nanostructures

F.K. Olsen[a,*], A.D. Bang[a], E. Digernes[a], S.D. Slöetjes[a,b], A. Scholl[b], R.V. Chopdekar[b], T. Tybell[a], J.K. Grepstad[a], E. Folven[a]

[a] Department of Electronic Systems, NTNU – Norwegian University of Science and Technology, 7491 Trondheim, Norway
[b] Advanced Light Source, Lawrence Berkeley National Laboratory, Berkeley, CA 94720, USA

ARTICLE INFO

Keywords:
Nanomagnets
LSMO
Patterned magnetic thin films
XMCD-PEEM

ABSTRACT

When thin films are patterned to realize nanoscale device geometries, maintaining their structural integrity is key to the quality of their functional properties. The introduction of new surfaces and interfaces by lateral modifications may alter material properties as well as the expected device functionality. In this study, two different techniques for nanoscale patterning of epitaxial thin films of $La_{0.7}Sr_{0.3}MnO_3$ are used to investigate the effects on their ferromagnetic properties and film crystalline structure. Nanomagnets are realized as free-standing structures and embedded ferromagnets in a paramagnetic matrix, respectively. We find that the magnetic dichroism signal in x-ray spectomicroscopy is stronger along the edges of the embedded magnets close to T_C. X-ray-diffraction measurements reveal a reduction of their in-plane lattice parameters. We discuss how in-plane stress from the nanomagnet surroundings can affect the magnetic properties in these structures.

1. Introduction

Thin film patterning is essential to the fabrication of modern electronic devices. Lithographic patterning techniques relying on etching or ion bombardment can be used to realize precisely controlled nanoscale structures [1]. However, when introducing new interfaces and surfaces on this length scale, the material properties may be perturbed. Locally, modifications of crystal and orbital structure can lead to substantial changes of functional properties such as conductivity, ferroelectricity, and magnetic order [2]. However, such changes brought about by patterning can also be exploited as a means of controlling material properties [3–5].

The strongly correlated electrons found in complex oxides imply a robust structure–property coupling, which make them good candidates for functional property engineering [2,6]. The ferromagnetic mixed-valence manganites are renowned for their metallic and magnetic nature resulting from the double-exchange mechanism [7]. Ferromagnetic $La_{0.7}Sr_{0.3}MnO_3$ (LSMO) has the highest Curie temperature (T_C) (370 K) of the manganites, shows a very large magnetoresistance dubbed colossal magnetoresistance (CMR), and has 100% spin polarization at the Fermi level [8–10]. The synthesis of high-quality thin films of LSMO by epitaxial growth on (001)-oriented $SrTiO_3$ (STO) substrates is well established [11–13]. However, tensile strain due to lattice mismatch with the STO substrate causes a reduced $T_C \sim 350$ K. This reduction in T_C has been explained in terms of a biaxial lattice distortion that increases the Jahn-Teller effect, which in turn inhibits the double exchange mechanism [14]. Furthermore, the magnetic properties of LSMO were shown to depend on parameters such as Sr content [8], oxygen stoichiometry [15], pressure [16] and strain [17]. Kozlenko et al. [16] showed that hydrostatic pressure increases the Curie temperature of LSMO, raising the question of whether this finding can be utilized to tailor the magnetic properties of nanomagnets defined in LSMO thin films.

In this study, we report on the magnetization of patterned LSMO thin film nanomagnets grown epitaxially on STO. Two different patterning techniques were adopted to realize nanomagnets embedded in a paramagnetic matrix and free-standing structures, respectively. X-ray photoemission electron microscopy measurements in combination with magnetic circular dichroism (XMCD-PEEM) were used to probe the magnetic domain structure of the patterned nanomagnets. Furthermore, x-ray diffraction (XRD) measurements on extended arrays of parallel lineshaped nanomagnets were carried out to probe the in-plane lattice parameters parallel and perpendicular to the lines.

* Corresponding author.
E-mail address: fredrik.k.olsen@ntnu.no (F.K. Olsen).

https://doi.org/10.1016/j.jmmm.2020.167324
Received 28 May 2020; Received in revised form 12 July 2020; Accepted 12 August 2020
Available online 26 August 2020

2. Experimental

Epitaxial films of LSMO, 90 unit cells (~35 nm) thick, were grown on 10 × 10 × 0.5 mm^3 Nb-doped (0.05 wt%) STO substrates by pulsed laser deposition. LSMO was deposited at 700°C in an oxygen ambient of 0.35 mbar using a KrF excimer laser with a pulse frequency of 1 Hz and a fluency of ~ 2 J/m^2. The target-to-substrate distance was 45 mm. *In situ* reflection high energy electron diffraction showed monolayer oscillations throughout the growth. After deposition, the films were annealed at the growth temperature in a 100 mbar oxygen atmosphere for 15 min. Each film was subsequently cut into four pieces. One piece was kept as a blanket (non-patterned) reference sample. Magnetization data from the reference samples was aquired using a Quantum Design vibrating sample magnetometer (VSM). The other three pieces were patterned into nanoscale thin film magnets. Masks were defined with electron beam lithography using a positive resist (CSAR62), then followed by Ar^+ ion implantation for fabrication of embedded magnetic structures, or by ion milling, using a mixture of Ar^+ and O^{2-} ions, for fabrication of free-standing magnets. The fabrication details are reported elsewhere [18]. For the patterned samples, two different designs were realized. Rectangular nanomagnets (2 × 0.8 μm^2 for embedded and 2 × 1 μm^2 for free standing) were prepared for magnetic domain imaging, and extended arrays (2.5 × 2.5 mm^2) of parallel lines, 500 nm wide with a pitch of 1 μm, were prepared for XRD measurements. Additionally, one sample was patterned with thinner embedded lines, 300 nm wide with a pitch of 600 nm. In the presented work, we will describe the crystalline orientations in terms of pseudocubic lattice parameters. All nanostructures were defined with their long axis parallel to in-plane ⟨110⟩ crystalline axes, which are the magnetic easy axes in (001)-oriented LSMO thin films [19]. The magnetic domain structure was imaged using the PEEM-3 microscope at the Advanced Light Source. The XMCD-PEEM images were measured at the Mn L_3 absorption edge with the x-rays incident at 30° with the sample surface parallel to the nanomagnets' long axis. Surface topography images were acquired using a Veeco Multimode V atomic force microscope, and the XRD measurements were taken with a Bruker D8 x-ray diffractometer.

3. Results

Fig. 1 shows schematics, AFM images, and AFM line scans of the embedded rectangular magnets [Fig. 1(a)] and the arrays of free-standing extended line magnets [Fig. 1 (b)]. The AFM linescan in Fig. 1(a) of a rectangular nanomagnet shows the characteristic topography of the embedded structures, i.e., well-defined nanomagnets with a ~6 nm height increase of the surrounding implanted regions. This difference is attributed to swelling as result of the Ar^+ ion implantation and is consistent with previous reports using this patterning technique [20,21]. Both AFM micrographs show little surface roughness. The topography of the free-standing structures appears from the AFM line scan of the extended line magnets in Fig. 1(b) and show well-defined parallel lines with a steep sidewall profile. The lines are 460 ± 40 nm wide with trenches 50–60 nm deep, exceeding the LSMO film thickness of 35 nm. The reduction in line-width relative to the nominal 500 nm width is attributed to over-exposure of the positive electron beam resist. Fig. 1(c) shows the temperature dependence of the saturation magnetization in a reference blanket LSMO film, as measured by VSM. The magnetization curve shows expected LSMO behaviour [22], and T_C is estimated at 345 K. Fig. 1(d) shows an XMCD-PEEM image of a rectangular nanomagnet recorded at 330 K. The arrows indicate how the direction of the magnetization is related to the contrast. In all presented XMCD-PEEM data, the direction of the incoming light is horizontal from left to right in the figures. We note that while magnetization parallel or antiparallel to the incoming light is clearly distinguishable, perpendicular oriented magnetization cannot be distinguished from the paramagnetic matrix surrounding the nanomagnet. As XMCD-PEEM is a surface sensitive technique, the signal is obtained from the top ~5 nm

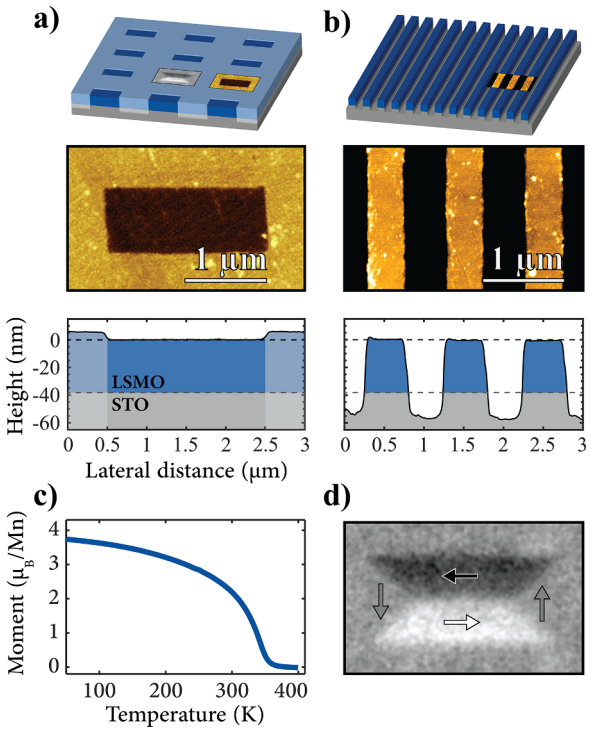

Fig. 1. Schematics, atomic force microscopy images and corresponding line scans of a) embedded rectangular magnets and b) free-standing lines. The color scale in the two AFM images is normalized to the max/min values for the scan in a). c) Saturation magnetization as function of temperature for a blanket LSMO film, measured in an applied field of 200 mT from 50 to 400 K. d) XMCD-PEEM image of a rectangular magnet recorded at 330 K. The arrows indicate the magnetization direction.

of the 35 nm thick film. It should also be noted that the temperatures is not measured at the sample surface in the VSM and PEEM-3 setups. Thus, a slight discrepancy between the measured temperatures is to be expected.

Fig. 2(a) shows XMCD-PEEM images of the embedded nanomagnets at temperatures near T_C. At 330 K, the magnetic domain patterns are clearly visible and take the form of a single or double Landau flux-closure, characteristic of rectangular magnets this size [23–25]. Upon heating the sample to 345 K, i.e., the T_C measured by VSM for the non-structured film, the overall dichroism signal is strongly reduced. Strikingly, at this temperature the XMCD-PEEM images show a stronger dichroism signal along the edges of the nanomagnets compared to that of their interior. The enhanced signal extends inwards from the edges ~150 nm, where the dichroism signal becomes indistinguishable from the surrounding paramagnetic matrix. When increasing the temperature to 360 K, the magnetic contrast along the edges disappears as the LSMO nanostructures rise above T_C. Magnetization is recovered upon subsequent lowering of the temperature to 330 K, with every rectangular nanomagnet entering a single flux-closure domain state.

XMCD-PEEM data for the rectangular free-standing nanomagnets is shown in Fig. 2(b). No enhanced dichroism signal is found along the nanostructure edges in such magnets for temperatures close to T_C. This suggests that the presence of a surrounding matrix is important to the enhanced dichroism signal near the edges of the embedded structures. We note, however, that the magnetic dichroism signal disappears at significantly lower temperature for the free-standing magnets than for the embedded magnets. X-ray absorption spectra taken on and in-between the magnets are compared in Fig. 2. For the free-standing magnets a distinct Mn^{2+} signal is obtained [26], indicating a reduced oxygen content in this sample [27]. It is well established that oxygen deficiency weakens the ferromagnetic properties in LSMO [12]. As the

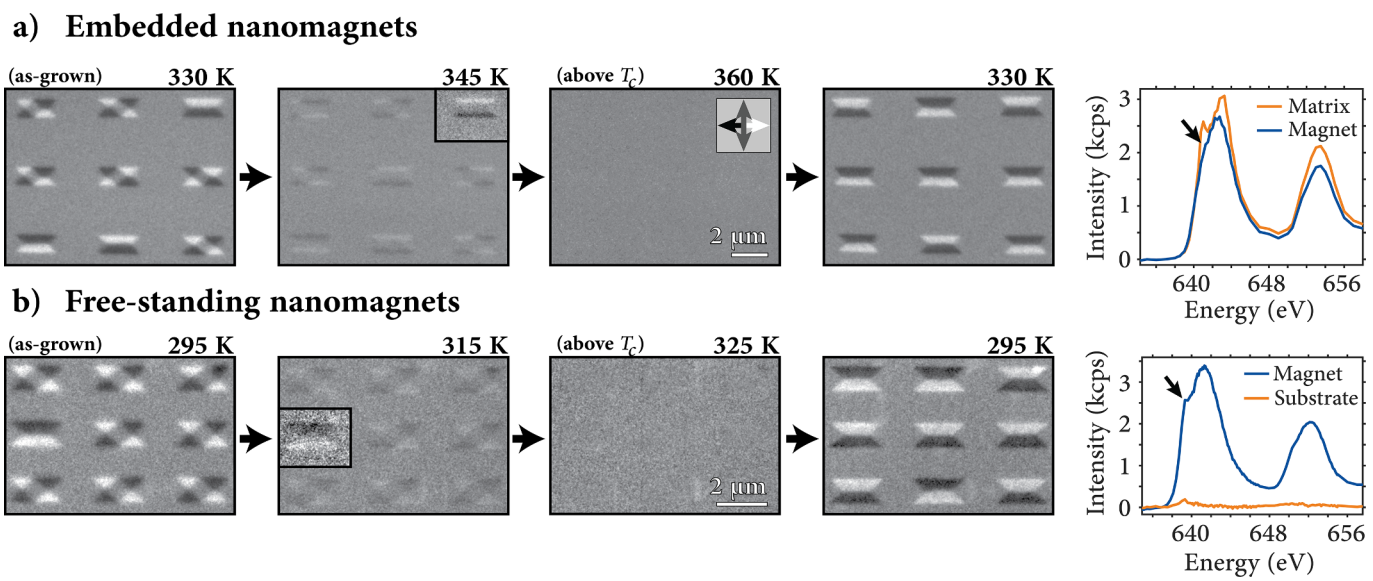

Fig. 2. X-ray photoemission electron microscopy images of a) embedded and b) free-standing nanomagnets recorded at temperatures around T_C in chronological order. The contrast is normalized to that measured at 330 K for embedded and at 295 K for free-standing nanomagnets. Marked with a black frame in the second column of images are magnets shown with maximized contrast for these selected structures. X-ray absorption spectra recorded on and in-between the magnets are shown on the right. The arrows in these graphs indicate the position of the Mn^{2+} peak.

films were grown using the same conditions for both samples, it is likely that the loss of oxygen is caused by the patterning process for the etched, free-standing samples. In particular, the ion milling process tends to harden the resist mask, and the following resist removal can be difficult. Thus, multiple exposures to the developing chemicals were required in the process and it is not unlikely that this processing causes some loss of oxygen in the LSMO thin film.

Upon close inspection of the magnetic dichroism signal near T_C for the embedded nanomagnets, we note an evolution of the domain structure for magnets with double flux-closures at the outset. XMCD-PEEM images of three selected rectangular magnets are shown in Fig. 3. At 330 K, the two flux-closures in each magnet are similar in size, and the domain wall positions along the edges are kept in place by the vortex structures. As the temperature increases to 340 K, the XMCD contrast in the central part of the magnets fades, and at 345 K magnetic contrast can be discerned along the nanomagnets' edges, only. Concurrent with the loss of magnetic contrast in the central part of the magnets, we find a change in domains near the nanomagnet edges – one of the two domains along the horizontal edges grows at the expense of the other. This finding indicates that the magnetic order in the central part of the magnets is lost, or at least too weak, to keep the domain walls stable along the edge at 345 K. After heating to 360 K and subsequently cooling to 330 K, a single flux-closure domain pattern appears in all nanomagnets. This observation implies that the magnet's

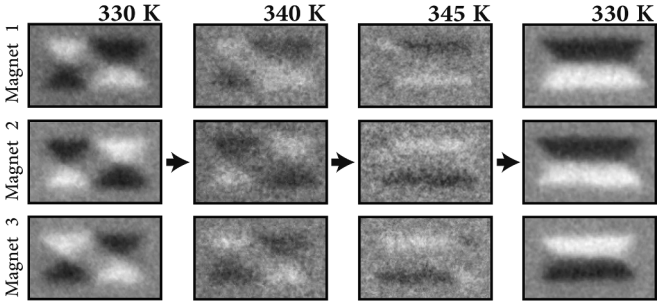

Fig. 3. X-ray photoemission electron microscopy images of three selected rectangular nanomagnets, showing an evolution in the domain pattern with increased temperature. The image contrast is normalized separately for each temperature.

edges, as well as their central sections have been heated above the magnetic ordering temperature.

A possible explanation for the enhanced dichroism signal along the edges of embedded nanomagnets is lateral stress imposed by the surrounding ion-implanted paramagnetic matrix, which the AFM investigation showed to be swollen. The dependence of T_C on isotropic pressure for LSMO was tested by Kozlenko et al. [16] and estimated at 4.3 K/GPa. In order to explore lateral pressure-induced changes in the LSMO lattice parameters for our patterned thin films, samples with extended arrays of parallel lines were investigated using XRD. In the following, the [110] direction is defined to be parallel to the patterned lines. The in-plane lattice parameters parallel and perpendicular to the lines were probed by recording reciprocal space maps (RSM) around {113} reflections. The {113} planes have $\vec{d}_{hkl}$ in-plane components along the ⟨110⟩ directions, i.e., either [110] which is parallel, or [1$\bar{1}$0] which is perpendicular to the lines. Schematic of the XRD geometry and the RSMs taken around the {113} peaks are shown in Fig. 4. The reference blanket film displays similar RSMs for all of the four equivalent {113} planes. Therefore, only one reference map is depicted in Fig. 4. The blanket film has the LSMO film peak aligned with that of the STO in the [hk0] direction, i.e., the film is fully strained to the substrate. The position of the LSMO peak in the [00l] direction corresponds to an out-of-plane (pseudocubic) lattice parameter of ~ 3.85 Å. This number is in accordance with reported parameters for epitaxial films of (001)-oriented LSMO/STO [11,28]. The diffuse peaks observed on either side of the LSMO film peak in the blanket film can be attributed to the presence of a 4-variant monoclinic structural distortion due to symmetry mismatch between rhombohedral LSMO and cubic STO [29].

Fig. 4 (b-d) show RSMs measured around the (113) peak for the patterned samples. The LSMO film peaks show no shift in the [hk0] direction, i.e., no change in the in-plane strain along the lines. However, the film peak is shifted towards the STO peak in the [00l] direction, indicating a larger out-of-plane lattice parameter compared to blanket films. The shift corresponds to a change in lattice parameter of 0.01 Å (~0.3%) for 500 nm wide lines and of 0.02 Å (~0.5%) for 300 nm wide lines. The signal-to-noise ratio is reduced compared to that recorded for blanket film samples. We note that a reduction in the signal-to-noise ratio is expected after patterning, as half the volume of the LSMO probed is either rendered amorphous (embedded line arrays) or removed (free-standing line arrays).

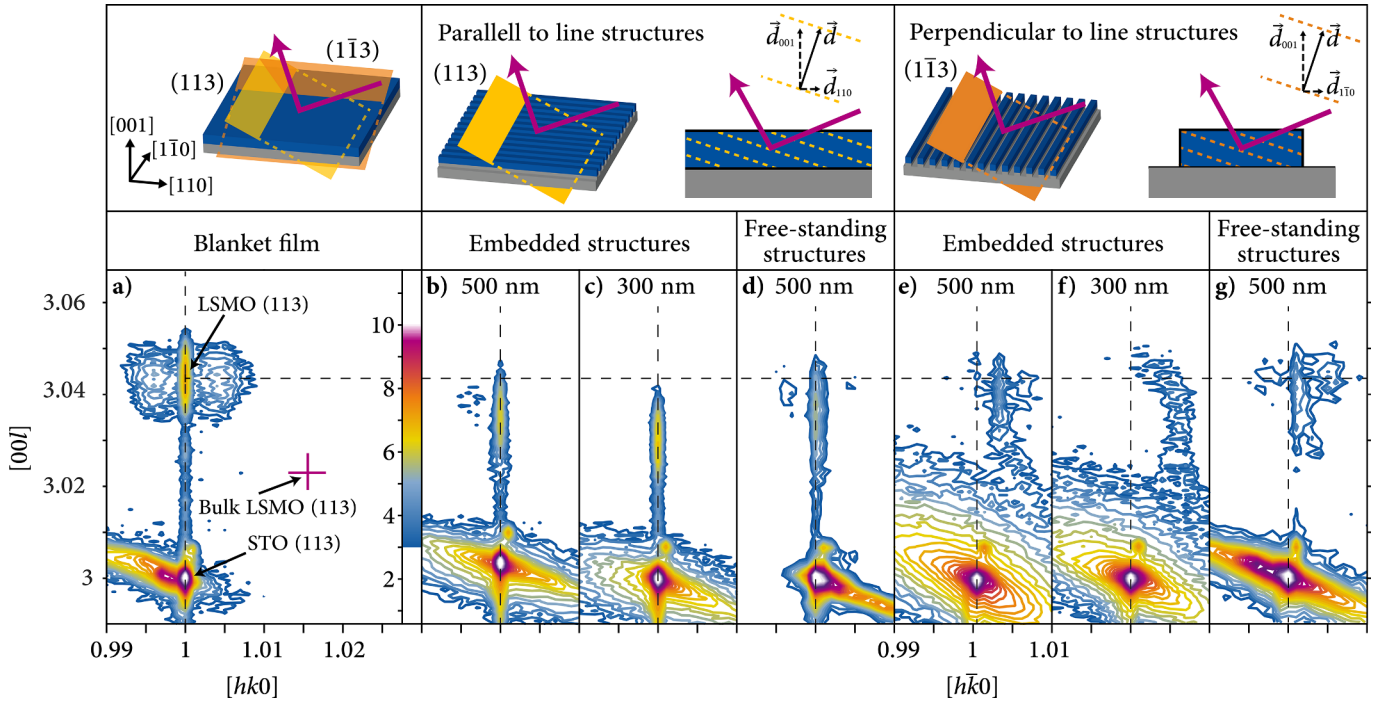

Fig. 4. XRD experimental geometry and reciprocal space maps recorded around the STO (113) diffraction peaks for a blanket film sample (a) and patterned structures (b-g). The scale on the x- and y-axes is given in units of *hkl* reciprocal lattice vectors. Dashed lines are introduced as a guide to the eye, indicating the film peak position for the blanket film. The position of the bulk LSMO (113) diffraction peak is indicated in a) for reference. The intensity scale is in ln(cps).

The RSMs of the (1$\bar{1}$3) diffraction peaks for the embedded line structures [Fig. 4 (e,f)] show a significant shift of the LSMO film peaks along [$h\bar{k}$0]. No overlap of the film and STO diffraction peaks is found in the in-plane direction. This suggests relaxation of the (1$\bar{1}$3) lattice parameter across the full linewidth. The shift along [$h\bar{k}$0] suggests that the LSMO pseudocubic unit cell is compressed along the [1$\bar{1}$0] direction, i.e., perpendicular to the patterned lines, while remaining fully strained to STO along the lines. For the fully strained blanket film the unit cell face diagonal is 5.523 Å. For the 500 nm lines it is reduced by 0.02 Å (~0.4%), and for the 300 nm lines, the reduction is 0.03 Å (~0.5%). Furthermore, the (1$\bar{1}$3) film peaks are found to be broadened and have a reduced amplitude compared to that found for (113). This finding suggests a slight variation of the LSMO lattice parameter in the in-plane direction across the line structures. The observation of one single peak rather than two, which one could expect from the XMCD-PEEM data, indicates that the lattice is distorted throughout the full width of both the 500 nm and the 300 nm lines. Since the line structures are only 500 nm and 300 nm wide, and the rectangles measured in XMCD-PEEM are 1 μm wide, it is not unlikely that the extension of strain imposed at the edges can be different. For the out-of-plane lattice parameter, a shift of the (1$\bar{1}$3) film peak towards the STO peak is observed for both linewidths, in keeping with the (113) RSM data. A minor shift of the diffraction peaks in-plane along [$h\bar{k}$0] can also be discerned for the (1$\bar{1}$3) RSMs of free-standing lines [Fig. 4 (g)], corresponding to a reduction of the pseudocubic unit cell along [1$\bar{1}$0] by 0.006 Å (~0.1%). This shift suggests that formation of free-standing lines also leads to relaxation of the tensile-strained LSMO film. However, the effect is much reduced compared to that observed for embedded structures.

From the XRD data summarized above, it is evident that the crystal structure of LSMO is affected by the patterning process. In particular, the embedded line magnets display an anisotropic modification of the in-plane lattice parameters. All the RSM data is consistent with an increase in the out-of-plane lattice parameter compared to blanket films, which may be expected from the measured relaxation of the in-plane epitaxial strain perpendicular to the nanomagnet lines. The XRD data is consistent with local stress imposed on the microstructures by swelling of the ion-implanted matrix. In bulk LSMO, Young's modulus is reported to be ~120 GPa [30,31]. Using the data from 300 nm wide lines, a change in lattice parameters of 0.5% would correspond to a pressure 0.6 GPa imposed on the line magnet sidewalls. With the pressure dependence of T_C reported by Kozlenko et al. [16], the corresponding increase in T_C would come to ~ 3 K, which is reasonably consistent with the XMCD-PEEM data. However, the variation in T_C with in-plane stress for nanostructured epitaxial films may differ from that of bulk LSMO for several reasons, such as the biaxial tensile strain from the substrate and the additional anisotropic distortion of the film crystalline structure.

4. Conclusions

In summary, the impact of two different patterning methods on the magnetic and structural properties of nanostructured thin films of LSMO was investigated. In particular, we report an increased magnetic dichroism signal near T_C along the edges of embedded nanomagnets, extending laterally ~150 nm inwards from the magnet edges. XRD measurements show that the patterning process leads to an anisotropic change of in-plane lattice parameters for line-shaped LSMO nanomagnets, notably a smaller lattice parameter perpendicular to the magnet-matrix interface. We argue that the enhanced dichroism signal can be attributed to lateral stress from swelling of the paramagnetic matrix surrounding the embedded nanomagnets upon Ar^+ ion implantation, and corresponding modification of the LSMO lattice parameters.

CRediT authorship contribution statement

F.K. Olsen: Conceptualization, Investigation, Formal analysis, Data curation, Visualization, Validation, Writing - original draft. **A.D. Bang:** Investigation. **E. Digernes:** Investigation. **S.D. Slöetjes:** Investigation. **A. Scholl:** Resources, Software. **R.V. Chopdekar:** Resources, Software. **T. Tybell:** Conceptualization, Writing - review & editing. **J.K. Grepstad:** Conceptualization, Writing - review & editing. **E. Folven:** Conceptualization, Project administration, Funding acquisition,

Supervision, Validation, Writing - review & editing.

Declaration of Competing Interest

The authors declare that they have no known competing financial interests or personal relationships that could have appeared to influence the work reported in this paper.

Acknowledgements

A special thanks to Kristoffer Kjærnes for fruitful discussions on XRD. The Advanced Light Source is supported by the Director, Office of Science, Office of Basic Energy Sciences, of the US Department of Energy under Contract No. DE-AC02-05CH11231. Nanoscale patterning and AFM imaging was carried out at NTNU NanoLab, NorFab. The Research Council of Norway is acknowledged for support to the Norwegian Micro- and Nanofabrication Facility, NorFab, Project No. 245963/F50. Partial funding was obtained from the Norwegian Ph.D. Network on Nanotechnology for Microsystems, which is sponsored by the Research Council of Norway, Division for Science, under Contract No. 221860/F60.

References

[1] J.I. Martin, J. Nogues, K. Liu, J.L. Vicent, I.K. Schuller, Ordered magnetic nanostructures: fabrication and properties, J. Magn. Magn. Mater. 256 (2003) 449–501, https://doi.org/10.1016/S0304-8853(02)00898-3.

[2] H.Y. Hwang, Y. Iwasa, M. Kawasaki, B. Keimer, N. Nagaosa, Y. Tokura, Emergent phenomena at oxide interfaces, Nature Mater. 11 (2012) 103–113, https://doi.org/10.1038/Nmat3223.

[3] S.N. Kim, Y.J. Nam, Y.D. Kim, J.W. Choi, H. Lee, S.H. Lim, Formation of magnetic anisotropy by lithography, Sci. Rep. 6 (2016), https://doi.org/10.1038/srep26709.

[4] N. Martin, J. McCord, A. Gerber, T. Strache, T. Gemming, I. Monch, N. Farag, R. Schafer, J. Fassbender, E. Quandt, L. Schultz, Local stress engineering of magnetic anisotropy in soft magnetic thin films, Appl. Phys. Lett. 94 (2009), https://doi.org/10.1063/1.3079664.

[5] B.M. Lefler, T. Duchon, G. Karapetrov, J.Y. Wang, C.M. Schneider, S.J. May, Reconfigurable lateral anionic heterostructures in oxide thin films via lithographically defined topochemistry, Phys. Rev. Mater. 3 (2019), https://doi.org/10.1103/PhysRevMaterials.3.073802.

[6] M. Lorenz, M.S.R. Rao, T. Venkatesan, E. Fortunato, P. Barquinha, R. Branquinho, D. Salgueiro, R. Martins, E. Carlos, A. Liu, F.K. Shan, M. Grundmann, H. Boschker, J. Mukherjee, M. Priyadarshini, N. DasGupta, D.J. Rogers, F.H. Teherani, E.V. Sandana, P. Bove, K. Rietwyk, A. Zaban, A. Veziridis, A. Weidenkaff, M. Muralidhar, M. Murakami, S. Abel, J. Fompeyrine, J. Zuniga-Perez, R. Ramesh, N.A. Spaldin, S. Ostanin, V. Borisov, I. Mertig, V. Lazenka, G. Srinivasan, W. Prellier, M. Uchida, M. Kawasaki, R. Pentcheva, P. Gegenwart, F.M. Granozio, J. Fontcuberta, N. Pryds, The 2016 oxide electronic materials and oxide interfaces roadmap, J. Phys. D 49 (2016), https://doi.org/10.1088/0022-3727/49/43/433001.

[7] C. Zener, Interaction between the *d*-shells in the transition metals. II. Ferromagnetic compounds of manganese with perovskite structure, Phys. Rev. 82 (1951) 403–405, https://doi.org/10.1103/PhysRev.82.403.

[8] A. Urushibara, Y. Moritomo, T. Arima, A. Asamitsu, G. Kido, Y. Tokura, Insulator-metal transition and giant magnetoresistance in $La_{1-X}Sr_xMnO_3$, Phys. Rev. B 51 (1995) 14103–14109, https://doi.org/10.1103/PhysRevB.51.14103.

[9] Y. Tokura, Y. Tomioka, Colossal magnetoresistive manganites, J. Magn. Magn. Mater. 200 (1999) 1–23, https://doi.org/10.1016/S0304-8853(99)00352-2.

[10] M. Bowen, M. Bibes, A. Barthelemy, J.P. Contour, A. Anane, Y. Lemaitre, A. Fert, Nearly total spin polarization in $La_{2/3}Sr_{1/3}MnO_3$ from tunneling experiments, Appl. Phys. Lett. 82 (2003) 233–235, https://doi.org/10.1063/1.1534619.

[11] A. Monsen, J.E. Boschker, F. Macia, J.W. Wells, P. Nordblad, A.D. Kent, R. Mathieu, T. Tybell, E. Wahlström, Thickness dependence of dynamic and static magnetic properties of pulsed laser deposited $La_{0.7}Sr_{0.3}MnO_3$ films on $SrTiO_3$(001), J. Magn. Magn. Mater. 369 (2014) 197–204, https://doi.org/10.1016/j.jmmm.2014.06.038.

[12] M. Huijben, L.W. Martin, Y.-H. Chu, M.B. Holcomb, P. Yu, G. Rijnders, D.H.A. Blank, R. Ramesh, Critical thickness and orbital ordering in ultrathin $La_{0.7}Sr_{0.3}MnO_3$ films, Phys. Rev. B 78 (2008), https://doi.org/10.1103/PhysRevB.78.094413.

[13] J.E. Boschker, E. Folven, A.F. Monsen, E. Wahlstrom, J.K. Grepstad, T. Tybell, Consequences of high adatom energy during pulsed laser deposition of $La_{0.7}Sr_{0.3}MnO_3$, Cryst. Growth Des. 12 (2012) 562–566, https://doi.org/10.1021/cg201461a.

[14] A.J. Millis, T. Darling, A. Migliori, Quantifying strain dependence in “colossal” magnetoresistance manganites, J. Appl. Phys. 83 (1998) 1588–1591, https://doi.org/10.1063/1.367310.

[15] J. Dho, N.H. Hur, I.S. Kim, Y.K. Park, Oxygen pressure and thickness dependent lattice strain in $La_{0.7}Sr_{0.3}MnO_3$ films, J. Appl. Phys. 94 (2003) 7670–7674, https://doi.org/10.1063/1.1628831.

[16] D.P. Kozlenko, I.N. Goncharenko, B.N. Savenko, V.I. Voronin, High pressure effects on the crystal and magnetic structure of $La_{0.7}Sr_{0.3}MnO_3$, J. Phys.-Condens. Mat. 16 (2004) 6755–6762, https://doi.org/10.1088/0953-8984/16/37/011.

[17] F. Tsui, M.C. Smoak, T.K. Nath, C.B. Eom, Strain-dependent magnetic phase diagram of epitaxial $La_{0.67}Sr_{0.33}MnO_3$ thin films, Appl. Phys. Lett. 76 (2000) 2421–2423, https://doi.org/10.1063/1.126363.

[18] A.D. Bang, I. Hallsteinsen, R.V. Chopdekar, F.K. Olsen, S.D. Sloetjes, K. Kjaernes, E. Arenholz, E. Folven, J.K. Grepstad, Shape-imposed anisotropy in antiferromagnetic complex oxide nanostructures, Appl. Phys. Lett. 115 (2019), https://doi.org/10.1063/1.5116806.

[19] L.M. Berndt, V. Balbarin, Y. Suzuki, Magnetic anisotropy and strain states of (001) and (110) colossal magnetoresistance thin films, Appl. Phys. Lett. 77 (2000) 2903–2905, https://doi.org/10.1063/1.1321733.

[20] Y. Takamura, R.V. Chopdekar, A. Scholl, A. Doran, J.A. Liddle, B. Harteneck, Y. Suzuki, Tuning magnetic domain structure in nanoscale $La_{0.7}Sr_{0.3}MnO_3$ islands, Nano Lett. 6 (2006) 1287–1291, https://doi.org/10.1021/nl060615f.

[21] E. Folven, T. Tybell, A. Scholl, A. Young, S.T. Retterer, Y. Takamura, J.K. Grepstad, Antiferromagnetic Domain Reconfiguration in Embedded $LaFeO_3$ Thin Film Nanostructures, Nano Lett. 10 (2010) 4578–4583, https://doi.org/10.1021/nl1025908.

[22] F.K. Olsen, I. Hallsteinsen, E. Arenholz, T. Tybell, E. Folven, Coexisting spin-flop coupling and exchange bias in $LaFeO_3/La_{0.7}Sr_{0.3}MnO_3$ heterostructures, Phys. Rev. B 99 (2019), https://doi.org/10.1103/PhysRevB.99.134411.

[23] K.X. Xie, X.P. Zhang, W.W. Lin, P. Zhang, H. Sang, Magnetization splitting in Landau and diamond-domain structures: Dependence on exchange interaction, anisotropy, and size, Phys. Rev. B 84 (2011), https://doi.org/10.1103/PhysRevB.84.054460.

[24] A.D. Bang, F.K. Olsen, S.D. Sloetjes, A. Scholl, S.T. Retterer, C.A.F. Vaz, T. Tybell, E. Folven, J.K. Grepstad, Magnetic domain formation in ultrathin complex oxide ferromagnetic/antiferromagnetic bilayers, Appl. Phys. Lett. 113 (2018), https://doi.org/10.1063/1.5047271.

[25] S.D. Sloetjes, H.H. Urdahl, J.K. Grepstad, E. Folven, Tailoring the magnetic order in a supermagnetic metamaterial, AIP Adv. 7 (2017), https://doi.org/10.1063/1.4978319.

[26] M. Khan, E. Suljoti, A. Singh, S.A. Bonke, T. Brandenburg, K. Atak, R. Golnak, L. Spiccia, E.F. Aziz, Electronic structural insights into efficient MnO_X catalysts, J. Mater. Chem. A 2 (2014) 18199–18203, https://doi.org/10.1039/c4ta04185b.

[27] S.W. Jin, X.Y. Zhou, W.B. Wu, C.F. Zhu, H.M. Weng, H.Y. Wang, X.F. Zhang, B.J. Ye, R.D. Han, Vacancy defects in epitaxial $La_{0.7}Sr_{0.3}MnO_3$ thin films probed by a slow positron beam, J Phys. D. 37 (2004) 1841–1844, https://doi.org/10.1088/0022-3727/37/13/017.

[28] H. Boschker, M. Huijben, A. Vailionis, J. Verbeeck, S. van Aert, M. Luysberg, S. Bals, G. van Tendeloo, E.P. Houwman, G. Koster, D.H.A. Blank, G. Rijnders, Optimized fabrication of high-quality $La_{0.67}Sr_{0.33}MnO_3$ thin films considering all essential characteristics, J Phys. D. 44 (2011), https://doi.org/10.1088/0022-3727/44/20/205001.

[29] J.E. Boschker, A.F. Monsen, M. Nord, R. Mathieu, J.K. Grepstad, R. Holmestad, E. Wahlstrom, T. Tybell, In-plane structural order of domain engineered $La_{0.7}Sr_{0.3}MnO_3$ thin films, Philos. Mag. 93 (2013) 1549–1562, https://doi.org/10.1080/14786435.2012.747010.

[30] S. Giraud, J. Canel, Young's modulus of some SOFCs materials as a function of temperature, J. Eur. Ceram. Soc. 28 (2008) 77–83, https://doi.org/10.1016/j.jeurceramsoc.2007.05.009.

[31] G. Fehringer, S. Janes, M. Wildersohn, R. Clasen, Proton-conducting ceramics as electrode/electrolyte – materials for SOFCs: preparation, mechanical and thermal-mechanical properties of thermal sprayed coatings, material combination and stacks, J. Eur. Ceram. Soc. 24 (2004) 705–715, https://doi.org/10.1016/S0955-2219(03)00262-0.